AGU PUBLICATIONS

JGR

Journal of Geophysical Research: Solid Earth

RESEARCH ARTICLE
10.1002/2016JB012949

Scaling of seismicity induced by nonlinear fluid-rock interaction after an injection stop

L. Johann[1], C. Dinske[1], and S. A. Shapiro[1]

[1] Institute of Geophysics, Freie Universitaet Berlin, Berlin, Germany

Key Points:
- Derivation of a novel scaling law for the back front and triggering front of postinjection-induced seismicity
- Back front and triggering front are sensitive to nonlinearity and the Euclidean dimension of the seismic cloud
- Modeling and testing of the scaling laws for case studies including propped stimulated domains

Correspondence to:
L. Johann,
lisajohann@zedat.fu-berlin.de

Citation:
Johann, L., C. Dinske, and S. A. Shapiro (2016), Scaling of seismicity induced by nonlinear fluid-rock interaction after an injection stop, *J. Geophys. Res. Solid Earth*, *121*, 8154–8174, doi:10.1002/2016JB012949.

Received 24 FEB 2016
Accepted 3 NOV 2016
Accepted article online 8 NOV 2016
Published online 18 NOV 2016

Abstract Fluid injections into unconventional reservoirs, performed for fluid-mobility enhancement, are accompanied by microseismic activity also after the injection. Previous studies revealed that the triggering of seismic events can be effectively described by nonlinear diffusion of pore fluid pressure perturbations where the hydraulic diffusivity becomes pressure dependent. The spatiotemporal distribution of postinjection-induced microseismicity has two important features: the triggering front, corresponding to early and distant events, and the back front, representing the time-dependent spatial envelope of the growing seismic quiescence zone. Here for the first time, we describe analytically the temporal behavior of these two fronts after the injection stop in the case of nonlinear pore fluid pressure diffusion. We propose a scaling law for the fronts and show that they are sensitive to the degree of nonlinearity and to the Euclidean dimension of the dominant growth of seismicity clouds. To validate the theoretical finding, we numerically model nonlinear pore fluid pressure diffusion and generate synthetic catalogs of seismicity. Additionally, we apply the new scaling relation to several case studies of injection-induced seismicity. The derived scaling laws describe well synthetic and real data.

1. Introduction

Caused by the world's increasing energy demand, the exploitation of unconventional hydrocarbon reservoirs and operation of geothermal systems has become a large issue within the last decade. To enhance hydraulic transport properties, pressurized fluids are injected into the reservoir.

Although the nature of fluid migration in the subsurface, particularly during hydraulic fracturing, is still poorly understood, it is known that borehole fluid injections are often accompanied by microseismicity [see, e.g., *Healy et al.*, 1968; *Raleigh et al.*, 1972, 1976]. Analyzing spatiotemporal distributions of the observed seismic events, hydraulic transport properties of the reservoir rock can be characterized [see *Shapiro*, 2015].

In recent years, many studies have been conducted in order to describe fundamental processes that lead to microseismicity associated with reservoir activity. On the one hand, seismic events are observed during the production of hydrocarbons or of fluids at Enhanced Geothermal Systems (EGS) [e.g., *Segall*, 1989; *Grasso*, 1992; *Zoback and Zinke*, 2002; *Majer et al.*, 2007; *Van Wees et al.*, 2014]. On the other hand, the injection of fluids, as, for example, at geothermal sites or during hydraulic fracturing of hydrocarbon reservoirs, very frequently causes seismicity [*Raleigh et al.*, 1972; *Zoback and Harjes*, 1997; *Baisch and Vörös*, 2010; *Ellsworth*, 2013].

Early tests to understand the behavior of rocks at high stresses were performed by *Griggs* [1936], who also invented the so-called Griggs apparatus to study the deformation of a rocks sample under high pressure. *Terzaghi* [1936] was the first one to propose that rock failure is controlled by an effective stress, given by the principal stresses minus the pore fluid pressure. *Paterson and Wong* [2005] studied the strength of rocks under the influence of stress and pore fluid pressure further. They conducted triaxial laboratory experiments which reveal that shear failure can be predicted by using the Mohr-Coulomb failure criterion in the principal coordinate system.

Following Terzaghi's concept of effective stresses [*Terzaghi*, 1936], *Talwani and Acree* [1984] and *Zoback and Harjes* [1997] proposed that pore fluid pressure artificially increases in the reservoir as a result of the injection. This leads to a decrease of the effective normal stress, which might cause sliding along already critically stressed preexisting favorably oriented cracks and fractures.

According to *Langenbruch and Shapiro* [2014], the stress distribution in elastically heterogeneous and fractured rock masses can be highly heterogeneous. However, all its principal components are dominantly (and nearly equally) modified by the diffusion of pore fluid pressure p.

In turn, an anisotropic distribution of p is mainly caused by an anisotropic permeability of the rock. The spatiotemporal evolution of microseismicity is generally controlled by such an anisotropic nature. Given microseismic event locations, *Shapiro et al.* [1999] and *Hummel and Shapiro* [2013, 2016] attempted to estimate the permeability anisotropy by solving an inverse problem. To account for the hydraulic anisotropy in real data examples, we later use an effective isotropic medium transformation (see section 4) [*Hummel*, 2013].

Seismicity during extraction and production is understood to be linked to a modification of normal and shear stresses which act on preexisting faults [*Majer et al.*, 2007; *Suckale*, 2009]. The focus in this study will be only on injection-induced seismicity.

Since the number of works on injection-induced seismicity has increased within the last years, many competing ideas on seismicity-controlling processes have developed. *Healy et al.* [1968] were the first to directly link the spatiotemporal distribution of observed microseismicity during waste water injection at the Rocky Mountain Arsenal, USA, with the fluid injection. They assume that rocks contain a number of favorably oriented critically stressed fractures and cracks which can be reactivated by increasing pressures. Thus, they consider the reduction of the frictional strength of preexisting cracks and fractures by increasing pore fluid pressures to be the fundamental mechanism for seismicity.

Hsieh and Bredehoeft [1995] quantitatively studied the waste water injection at the Rocky Mountain Arsenal, USA, further. The authors show that the pressure buildup along the reservoir coincides with the spatial distribution of microseismic locations. Thus, *Hsieh and Bredehoeft* [1995] propose that seismicity is likely to be induced by the increased pore fluid pressure as already noted by *Healy et al.* [1968].

On the basis of comprehensive seismic monitoring of reservoir-induced seismicity in South Carolina, USA, *Talwani and Acree* [1984] suggest that the diffusion of pore fluid pressure plays a major role for the spatiotemporal distribution of microseismic events during fluid injections. They assume that seismicity mainly occurred on critically stressed preexisting fractures. With that idea they follow previous works as mentioned above. Furthermore, they use the spatiotemporal distribution of epicenters to get estimates of the hydraulic diffusivity.

The aforementioned works do not consider poroelastic effects as described in the pioneering work by *Biot* [1941], i.e., that a change of pore fluid pressure induces stresses, which in turn cause changes in pore fluid pressure. *Rutqvist et al.* [2008] performed a poroelastic analysis of reservoir-geomechanical modeling for tensile and shear failure at a CO_2 storage system. They show that the total horizontal compressive stress increases as a result of the injection, while total vertical stresses do not change significantly.

A poroelasticity-based study by *Rozhko* [2010] (see also discussion by *Shapiro* [2012]) revealed that shear stress changes can become larger than pore fluid pressure changes at locations far from the injection source.

Segall and Lu [2015] and *Chang and Segall* [2016] further examined processes that control fluid injection-induced seismicity. They show that pore fluid pressures predicted by a poroelastic model are larger than those predicted by pure diffusion models. Yet the pressure distribution strongly depends on the in situ stress regime of the reservoir. Moreover, they show that induced stresses can have a significant impact on injection-related seismicity, especially at large distances from the source.

However, poroelastic coupling parameters such as the Biot coefficient α used in the aforementioned studies are relatively high (e.g., $\alpha \geq 0.3$). These values are too high for situations in which fluids are injected into a rock formation which is characterized by initially isolated pores and nearly negligible permeability of the rock matrix. In such a situation, α is significantly smaller than previously reported values. As shown in chapters 2.9.5 and 3.4 in *Shapiro* [2015], the strength of the poroelastic stress coupling, controlled by parameter $n_s = \alpha n'$ [*Shapiro*, 2015, equation 2.277 with 2.278], with $\alpha \leq 0.3$ results in pore fluid pressure perturbations which dominate shear stress perturbations. Since the modeling performed in this study is based on a hydraulic fracturing treatment of a shale gas reservoir, we here neglect poroelastic coupling effects. Our study follows many other works [e.g., *Talwani and Acree*, 1984; *Shapiro et al.*, 1997, 1999; *King et al.*, 2016], by accepting the mechanism of pore fluid pressure diffusion as the underlying process of fluid-induced seismicity. Such a simplified model corresponds to a poroelastic analysis for situations with small α. This limit is fundamental for understanding

triggering processes as well. Below we provide an analytic solution for this case. Such a solution can be especially significant for situations where multiparameter description is possible and dominance of various effects is not clear. An analytical solution can then be used as an orientation to understand contribution of different phenomena, especially in future nonlinear poroelastic coupled models.

Based on the assumption of solely pore fluid pressure diffusion, *Shapiro et al.* [1997, 1999, 2002] developed a method for the determination of the hydraulic diffusivity D of the medium, known as the seismicity-based reservoir characterization. This approach spatiotemporally analyzes the distribution of microseismicity induced during the injection. Yet seismic activity is not restricted to the injection phase but occurs also after the termination of the fluid injection. *Parotidis et al.* [2004] studied this phenomenon further and observed an aseismic domain which evolves in time and space around the injection source after the injection stop at time $t = t_0$. The authors first introduced and analytically described the back front of seismicity, which can also be used for the quantification of hydraulic reservoir properties. Their description is based on the linear differential equation for pore fluid pressure diffusion.

All studies mentioned above [*Rutqvist et al.*, 2008; *Rozhko*, 2010; *Segall and Lu*, 2015; *Chang and Segall*, 2016] addressed linear effects only. This is an important feature of the corresponding poroelastic models. In many situations, the spatiotemporal distribution of seismicity is not captured by linear pore fluid pressure diffusion. One example is hydraulic fracturing, where hydraulic transport properties are significantly enhanced and become a function of pore fluid pressure. This observation correlates well with the understanding of hydraulic rock properties to be dependent on the effective stress. Numerous works, e.g., by *Katsube et al.* [1991], *Berryman* [1992], *Detournay and Alexander* [1993], *Al-Wardy and Zimmerman* [2004], *Li et al.* [2009], and *Shapiro et al.* [2015] show that hydraulic rock parameters such as the permeability can be strongly influenced by pore fluid pressure. Enhanced pore fluid pressure increases the size of pores. This effect may lead to a rather nonlinear pore fluid pressure diffusion process. In other words, the differential diffusion equation, effectively describing the process of pore fluid pressure perturbation, becomes strongly nonlinear.

To understand seismicity induced by nonlinear diffusion of pore fluid pressure, much work has recently been done [*Rice*, 1992; *Miller et al.*, 2004; *Shapiro and Dinske*, 2009; *Dinske*, 2010; *Hummel and Shapiro*, 2012; *Gischig and Wiemer*, 2013]. *Shapiro and Dinske* [2009] as well as *Hummel and Shapiro* [2012] found scaling relations for the triggering front of seismicity induced during the injection by nonlinear diffusion of pore fluid pressure for different sets of boundary conditions. These help to understand the controlling parameters and can be used for large-scale diffusivity estimates of the reservoir.

In this paper, we assume the pore fluid pressure perturbation as the triggering mechanism. We use the previously obtained results for rather general cases of nonlinear pore fluid pressure diffusion [see, e.g., *Shapiro and Dinske*, 2009; *Shapiro*, 2015] and formulate the front behavior for the postinjection-induced seismicity. We derive a novel theoretical scaling relation for the back front but also for the triggering front of seismicity after the injection stop. To verify the theoretical finding, comprehensive 3-D modeling of nonlinear pore fluid pressure diffusion is carried out. For this purpose, we generate catalogs of synthetic seismicity. We examine the spatiotemporal distribution of synthetic seismicity induced during as well as after the injection termination and compare observed scaling relations for the back front to theoretical values predicted by the novel scaling law. Additionally, we apply the theoretical relation to back front signatures of different hydraulic fracturing and Enhanced Geothermal System (EGS) case studies taken from literature. We show that the derived scaling law works well for real data. Therefore, the methodology can be used for further reservoir characterization, understanding of hydraulic fracturing processes as well as hazard assessment.

2. Theoretical Background

2.1. Linear Pore Fluid Pressure Diffusion

Fluid injections into the subsurface are frequently accompanied by microseismic activity. A probable triggering mechanism of observed microseismicity is the diffusion of pore fluid pressure. Approximating the fluid injection by a point source of pressure perturbation into an infinite hydraulically homogeneous and isotropic poroelastic fluid-saturated medium, the spatiotemporal evolution of the pore fluid pressure perturbation p can be found in Biot's equations. According to *Shapiro et al.* [1997, 1999, 2002], the diffusion equation for the low-frequency range can be expressed by

$$\frac{\partial p}{\partial t} = \nabla(D\nabla p)\,, \tag{1}$$

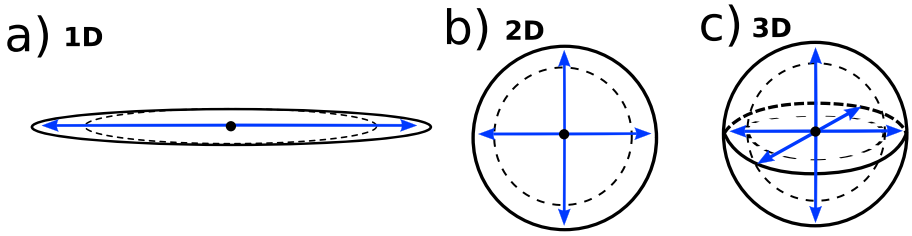

Figure 1. Euclidean dimensions of diffusion. (a) One-dimensional diffusion describes the diffusion along a typical hydraulic fracture and results in seismic clouds which occur on or in vicinity of this fracture. (b) The 2-D case indicates that the diffusion occurred in a plane, yielding a two-dimensional event distribution. (c) In 3-D, a hydraulic fracture interacts with a preexisting fracture network, which gives seismic events in 3-D space.

with the time t, pore fluid pressure p, and the scalar hydraulic diffusivity D, which is assumed to be constant in time and independent of pressure.

Dependent on the local stress field, mechanical and hydrological rock properties, and the injection pressure strength, the diffusion of pore fluid pressure can effectively occur in one, two, or three dimensions as shown in Figure 1. While the 1-D case describes the diffusion of pore fluid pressure along a typical hydraulic fracture, the two-dimensional example is valid for diffusion in a plane. In contrast, three-dimensional diffusion occurs in the case of the pressure perturbation propagating in a complex fracture network, for example, either opening of preexisting cracks and pores or new cracks and pores. Later, we address the 1-D, 2-D, and 3-D scenarios in more detail.

Shapiro et al. [1997, 1999, 2002] use the spatiotemporal event distribution for the characterization of the scalar hydraulic diffusivity D of a hydraulically effective isotropic medium. In r-t plots, where the radial event distance from the injection source r is plotted versus the event occurrence time t, the triggering front of seismicity can be found as an envelope of the seismic cloud. For an isotropic and homogeneous medium it is approximately given by the heuristic relation:

$$r_{\mathrm{tf}} = \sqrt{4\pi D t}\,. \tag{2}$$

The parameter D is directly related to the permeability k by $D = k/(\mu S)$. Here μ is the dynamic viscosity of the fluid and S denotes the storage coefficient defined by *Jaeger et al.* [2007, p. 188] which combines the porosity and different rock bulk moduli. Whereas most sandstones have permeabilities within the range of 10^{-16} to 10^{-12} m^2, the permeability of shales is usually much lower with values between 10^{-21} m^2 and 10^{-18} m^2 [*Hummel*, 2013].

Since fluid-induced seismicity is also observed after the injection stop, *Parotidis et al.* [2004] include spatiotemporal characteristics of postinjection-induced seismicity in reservoir characterization, specifically to get estimates of the hydraulic diffusivity D. As the study shown in this paper is only valid for injection-induced seismicity (see also section 1), we do not consider production-induced events which are associated with different physical mechanisms, namely, poroelastic stress changes [see, e.g., *Segall*, 1989; *Grasso*, 1992; *Zoback and Zinke*, 2002; *Majer et al.*, 2007; *Baisch and Vörös*, 2010; *Van Wees et al.*, 2014].

On the assumption that seismicity occurs only for increasing pore fluid pressures, an aseismic domain, evolving around the source after the pressure has reached its local maximum and $\frac{\partial p}{\partial t} \leq 0$, can be defined. *Parotidis et al.* [2004] documented observations on this domain. They call the lower (smaller-distance) boundary of postinjection-induced seismicity the back front of seismicity. For a hydraulically homogeneous and isotropic medium and a constant-rate fluid injection until $t = t_0$, *Parotidis et al.* [2004] used the analytical solution of the pressure distribution as given by *Carslaw and Jaeger* [1959] for event distances r at times $t > t_0$. In such a case, the lower boundary of seismicity can be described by the following exact result:

$$r_{\mathrm{bf}} = \sqrt{2dDt\left(\frac{t}{t_0} - 1\right)\ln\left(\frac{t}{t - t_0}\right)}. \tag{3}$$

Again, D is the hydraulic diffusivity of the rock and d is the Euclidean dimension of the space of seismic cloud dominant growth, influenced by the dimension of pore fluid pressure diffusion (Figure 1). The value for d is taken from the spatiotemporal distribution of seismic events. It is $d = 3$ for a 3-D cloud, $d = 2$ for a 2-D case,

i.e., a seismicity cloud evolving in time predominantly on a plane, and $d = 1$ for a 1-D case, i.e., seismicity occurring predominantly along a line or a thin spatial band. Fitting equations (2) and (3) to the seismic cloud yields estimates of the medium hydraulic diffusivity D. Given that seismicity is induced by linear pore fluid pressure diffusion in a hydraulically homogeneous medium, the values of D in equations (2) and (3) will coincide [see, e.g., *Parotidis et al.*, 2004; *Hummel and Shapiro*, 2016].

2.2. Nonlinear Pore Fluid Pressure Diffusion

In many situations, the diffusivity becomes a function of pore fluid pressure. This is always the case for hydraulic stimulations of reservoirs. High fluid pressure (comparable to or higher than the minimum principal stress σ_3) acts against the normal stress and increases apertures of pores and fractures. This leads to a strong enhancement of permeability and has been described and discussed in previous works [see, e.g., *Shapiro and Dinske*, 2009; *Hummel and Shapiro*, 2012; *Gischig and Wiemer*, 2013; *Miller*, 2015]. Approximating the fluid injection by a point source switched on at $t = 0$ s and neglecting hydraulic anisotropy and heterogeneity, the following general differential equation of diffusion can be derived for a d-dimensional space [*Shapiro and Dinske*, 2009]:

$$\frac{\partial p}{\partial t} = \nabla(D(p)\nabla p). \tag{4}$$

This equation describes the perturbation of pore fluid pressure in time and space, controlled by a pressure-dependent diffusivity $D(p)$. It can be applied for diffusion in 1-D, 2-D, and 3-D (see also Figure 1).

Later, we numerically model a 3-D diffusion scenario where the seismicity is induced by the pore fluid pressure diffusion. In contrast, our analytical results are valid for 1-D, 2-D, and 3-D geometries of a hydraulic stimulation (see Figure 1). In this case, the diffusion equation (equation (4)) describes pore fluid pressure perturbation propagating along a hydraulic-fractured domain. Due to pore fluid pressure perturbation and coupled stress changes in the surrounding rocks caused by the fracturing, seismic events are induced parallel to this propagating pressure perturbation, inside and behind the boundaries of the fractured domain.

To account for the pressure dependence, *Shapiro and Dinske* [2009] propose the following power law for the diffusivity [see also *Shapiro et al.*, 2015]

$$D(p) = (n+1)D_0 p^n\,, \tag{5}$$

where $D(p) = D(p(x, y, z, t))$. Thus, the diffusivity depends on pore fluid pressure p, which in turn is a function of location (x, y, z) and time t. Correspondingly, also, D is a function of location and time. Furthermore, n is the index of nonlinearity which describes the influence of nonlinear pore fluid pressure diffusion on transport properties. It may depend on reservoir properties such as lithology and pore space geometry. D_0 is a scaling parameter with unit $m^2/(s\ Pa^n)$, and $(n + 1)$ is an integration factor. While $n = 0$ describes the linear diffusion case, the diffusivity will strongly depend on pressure for large n. Since we consider the diffusion of pore fluid pressure as the seismicity controlling triggering mechanism, p is the changing variable and the tectonic stress remains almost unaffected. Thus, the effective normal stress is modified predominantly by p. Here we neglect poroelastic coupling of stress and pressure, which is an acceptable approximation in tight rocks (see section 1) [*Shapiro*, 2015, chap. 2].

If pore fluid pressure diffusion is controlled by nonlinear fluid-rock interaction, linear diffusion triggering front and back front (equations (2) and (3)), respectively) do not adequately describe the temporal behavior of the seismic cloud. Rather, equations (2) and (3) can be used to obtain heuristic effective diffusivity estimates D_h [*Hummel and Shapiro*, 2016]. If diffusion is controlled by a highly nonlinear process, $D_{h,\mathrm{tf}}$ for the triggering front and $D_{h,\mathrm{bf}}$ for the back front no longer coincide.

To determine the actual temporal dependence of the seismicity induced during as well as after the injection, we recall that we assume a power law dependence of the diffusivity. Power law functions are also possible simple fits to the seismic envelope [see, e.g., *Hummel and Shapiro*, 2012, 2016]. They can be empirically applied according to

$$r_{\mathrm{tf}} = At^{\chi} \tag{6}$$

for the triggering front and

$$r_{\mathrm{bf}} = B(t - t_0)^{\psi} \tag{7}$$

for the back front of seismicity. Later, we show that the power laws are indeed theoretically justified.

The parameters A, B, and χ, ψ are determined by a fit of functions (6) and (7) to the upper and lower boundaries of seismic clouds in corresponding *r-t* plots, respectively.

Shapiro and Dinske [2009] and *Hummel and Shapiro* [2012] demonstrate that the parameter χ takes values between 1/3 and 1/2. While a value of $\chi = 1/2$ indicates linear fluid-rock interaction, the lower limit of $\chi = 1/3$ is obtained for seismicity induced by very strong nonlinear diffusion ($n \to \infty$) of pore fluid pressure in 3-D media. In contrast, for the back front, $\psi \approx 1/3$ in case of linear pore fluid pressure diffusion, but it is significantly smaller than 1/3 for nonlinear pore fluid pressure diffusion [*Hummel and Shapiro*, 2016].

2.3. Scaling of the Triggering Front

Shapiro and Dinske [2009] found the parameters that control the temporal behavior of the triggering front by deriving a scaling law for times t before the injection stop at t_0. They assumed initially homogeneous and isotropic rocks and considered simplifications of equation (4) for a radially symmetric d-dimensional geometry with the diffusivity model formulated by equation (5) [see also *Shapiro*, 2015, equation (4.22)]

$$\frac{\partial r^{d-1} p}{\partial t} = D_0 \frac{\partial}{\partial r} r^{d-1} \frac{\partial}{\partial r} p^{n+1} . \tag{8}$$

Q_0 is a normalizing coefficient defining the fluid injection rate $Q_i(t)$ [*Shapiro*, 2015, p. 185]:

$$Q_i(t) = S(i+1) A_d Q_0 t^i . \tag{9}$$

In this equation, S is the storage coefficient and A_d will take values of 4π, $2\pi h$, and $2A_r$ for a d-dimensional space of $d = 3$, 2, or 1, respectively. h is the height of a hypothetical homogeneous plane layer for a cylindrically symmetric injection source ($d = 2$), and A_r denotes the cross section of a hypothetical infinite straight rod ($d = 1$). The parameter i depends on the injection source. It is $i = -1$ for a delta-like, instantaneous injection of a finite fluid volume and $i = 0$ in case of a constant injection rate. For a linearly with time increasing injection rate $i = 1$, which results in parabolic cumulative injected volume with time. For illustration of the injection source, see Figure 2.

Shapiro and Dinske [2009] show for the formulation of $Q_i(t)$ (equation (9)) that the mass conservation law leads to the following simple constraints [*Shapiro*, 2015, equation (4.23)]:

$$\int_0^\infty r^{d-1} p(t, r)\, \mathrm{d}r \; = \; Q_0 t^{i+1} . \tag{10}$$

This is an expression of the fact that the volume integral of the pore fluid pressure perturbation during an injection is proportional to the injected fluid volume. Using the conditions above, the authors performed a dimensional analysis of the quantities r, t, D_0, and Q_0 which influence the pressure perturbation [see also *Shapiro*, 2015, equations (4.22)–(4.23)]. The dimensions are given by $[r] = L$, $[t] = T$, $[D_0] = \frac{L^2}{T^{pn}}$, and $[Q_0] = \frac{PL^d}{T^{i+1}}$. From these quantities, only one dimensionless combination θ can be found. It is given by

$$\theta = r \left(D_0 Q_0^n t^{n(i+1)+1} \right)^{\frac{-1}{(dn+2)}} . \tag{11}$$

A combination of the quantities in equation (11) yields the dimension of pressure $p = [P]$:

$$\left(\frac{Q_0^2}{D_0^d t^{(d-2i-2)}} \right)^{\frac{1}{(dn+2)}} \tag{12}$$

Following the Π theorem as defined in *Barenblatt* [1996], a description of pressure can then be formulated as follows:

$$p(t, r) = \left(\frac{Q_0^2}{D_0^d t^{(d-2i-2)}} \right)^{1/(dn+2)} \Phi(\theta) . \tag{13}$$

Here $\Phi(\theta)$ is a dimensionless function found by substituting (5) and (13) into (8) and (10) and applying the boundary condition $p = 0$ Pa for $t < 0$ s [see *Shapiro*, 2015, equations (4.36)–(4.37)].

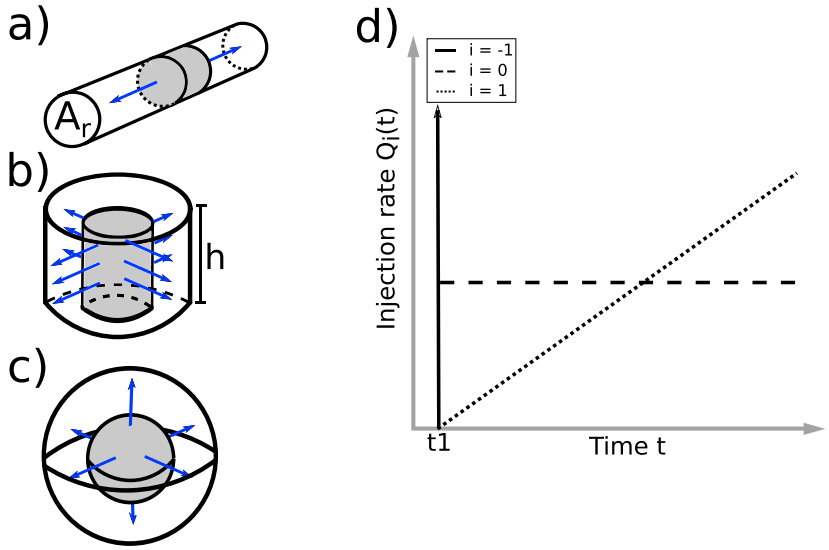

Figure 2. (a–c) The 1-D, 2-D, and 3-D injection scenarios. (d) The different geometries influence the injection rate $Q(t) = S(i+1)A_d Q_0 t^i$, where i denotes the injection type. It is $i = -1$ for an instantaneous injection of a finite volume of fluid, $i = 0$ for a constant injection, and $i = 1$ for an increasing injection rate. A_d takes values of $2A_r$, $2\pi h$, and 4π for $d = 1$, 2, and 3, respectively. Q_0 is a scaling parameter, and S is the storage coefficient. Visualized are functions for $i = -1$, 0, and 1 (solid, dashed, and dotted lines, respectively).

Further, rearranging (11) yields a general proportionality for the triggering front

$$r_{tf} \propto \left(D_0 Q_0^n t^{n(i+1)+1}\right)^{\frac{1}{(dn+2)}} . \tag{14}$$

Additionally, *Hummel and Shapiro* [2012] investigate triggering front signatures for a constant injection pressure source ($i = 0$). Their results show that χ in equation (6) is very well described by $\chi = (n+1)/(dn+2)$, what is in agreement with equation 14.

2.4. Scaling of Postinjection-Induced Seismicity

To understand the nature of postinjection-induced seismicity, we derive a novel scaling law for the back front of seismicity.

Let us assume that the observation time is significantly longer than the injection period. Then, we can further use the scaling laws introduced by *Shapiro and Dinske* [2009] for our theoretical derivation of the back front scaling law. For this we accept the assumption of an instantaneous injection of a finite fluid volume (i.e., $i = -1$). This permits to avoid consideration of a second time which corresponds to the instantaneous termination of the fluid injection, t_0. Furthermore, we take into account that the injection source corresponds to a point-like source at the radial distance $r = 0$ m. In this way, we will obtain asymptotic long time limit scaling laws for the triggering and back fronts, which can then be applied to real data examples of fluid-induced seismicity.

Under the above mentioned assumptions of $i = -1$ and a point-like (in d-dimensional space) injection source located at $r = 0$ m, equation (13) can be written as

$$p(t,0) = \left(\frac{Q_0^2}{D_0^d t^d}\right)^{1/(dn+2)} \Phi(0) , \tag{15}$$

where $\Phi(0)$ is a constant. Using the expression for the pressure distribution $p(t,0)$, equation (13) can be reformulated, yielding the pressure distribution at distances r smaller than the triggering front r_{tf} [*Shapiro and Dinske*, 2009; *Shapiro*, 2015]:

$$p(t,r) = p(t,0)\left(1 - \frac{r^2}{r_{tf}^2}\right)^{1/n} . \tag{16}$$

Please note that $p = 0$ if $r > r_{tf}$.

Assuming that events are only induced for increasing pore fluid pressure, the condition for the back front is given by the vanishing partial time derivative $\frac{\partial p(t,r)}{\partial t}$. Using equation (16) for computing this derivative, we get

$$\frac{\partial p(t,0)}{\partial t}\left(1-\frac{r^2}{r_{\mathrm{tf}}^2}\right)^{1/n}+\frac{2}{n}p(t,0)\left(1-\frac{r^2}{r_{\mathrm{tf}}^2}\right)^{(1-n)/n}\frac{r^2}{r_{tf}^3}\frac{\partial r_{\mathrm{tf}}}{\partial t}=0\,. \tag{17}$$

The partial time derivative of the pressure distribution $p(t,0)$ (equation (15)) is given by

$$\frac{\partial p(t,0)}{\partial t}=t^{d/(\mathrm{d}n+2)}\frac{1}{t}p(t,0)=\frac{-d}{\mathrm{d}n+2}t^{-1}p(t,0)\,. \tag{18}$$

Substituting equation (18) into equation (17) leads to the following criterion for the back front:

$$0=\frac{-d}{\mathrm{d}n+2}t^{-1}+\frac{2}{n}\left(1-\frac{r^2}{r_{\mathrm{tf}}^2}\right)^{-1}\frac{r^2}{r_{\mathrm{tf}}^3}\frac{\partial r_{\mathrm{tf}}}{\partial t}\,. \tag{19}$$

The solution $r(t)$ of this equation yields the back front $r_{\mathrm{bf}}=r(t)$.

Using $i=-1$ in equation (14), we get

$$r_{\mathrm{tf}}\propto\left(Q_0^nD_0t\right)^{1/(\mathrm{d}n+2)}\,. \tag{20}$$

The function $\partial r_{\mathrm{tf}}(t)/\partial t$ in equation (19) can be found from equation (20). It is given by

$$\frac{\partial r_{\mathrm{tf}}}{\partial t}\propto\frac{1}{\mathrm{d}n+2}\left(D_0Q_0^n\right)^{1/\mathrm{d}n+2}t^{-(\mathrm{d}n+1)/(\mathrm{d}n+2)}\,. \tag{21}$$

Subsequently, the combination of equations (20) and (21) yields (note that a proportionality constant in these equations is eliminated in this way)

$$\frac{1}{r_{\mathrm{tf}}}\frac{\partial r_{\mathrm{tf}}}{\partial t}=\frac{1}{\mathrm{d}n+2}t^{-1}\,. \tag{22}$$

Substituting this into equation (19) gives the following result:

$$\mathrm{d}n=(2+\mathrm{d}n)\frac{r^2}{r_{\mathrm{tf}}^2}\,, \tag{23}$$

where r is a function of time, describing the back front distance from the source, r_{bf}. Thus,

$$r_{\mathrm{bf}}(t)=r_{\mathrm{tf}}(t)\left(\frac{\mathrm{d}n}{2+\mathrm{d}n}\right)^{(1/2)}\,. \tag{24}$$

Using this relation in combination with equation (20), we finally obtain for the time scaling of the back front of seismicity:

$$r_{\mathrm{bf}}\propto t^{\frac{1}{2+\mathrm{d}n}}\,. \tag{25}$$

Therefore, seismicity induced by the relaxation of pore fluid pressure after the termination of the fluid injection shows a $t^{\frac{1}{2+\mathrm{d}n}}$ — proportionality of the back front distance r_{bf}. Since the asymptotic character of equations (18) to (25) is not maintained for $n=0$, equation (25) is not valid for linear pore fluid pressure diffusion.

Using the above made assumption of a long time limit, we note that the scaling given by equation (25) holds also for the triggering front:

$$r_{\mathrm{tf}}\propto t^{\frac{1}{2+\mathrm{d}n}}\,, \tag{26}$$

which can be applied for linear diffusion cases as well. Unlike equation (20), which is derived from equation (14) and therefore valid for all times, equation (26) applies only to the triggering front for long times after the injection stop.

Equations (24)–(26) have the following implications. In case of strong nonlinearity (high n), the time dependence of both fronts vanishes for long times; i.e., they both stabilize on a time-independent distance.

3. Modeling of Nonlinear Pore Fluid Pressure Diffusion

Since pressure-dependent diffusivities can be observed during proppant injections, such as hydraulic fracturing [*Mader*, 1989], and self-propping processes by shear dilatation, e.g., at geothermal sites [*Durham and Bonner*, 1994], the influence of this effect on injection-induced microseismic distributions needs to be further studied not only for coinjection times but also for the postinjection period.

To understand features of coinjection- and postinjection-induced microseismic events under the aforementioned conditions of changing pressure dependencies for the limiting poroelastic case of small Biot constants α (i.e., pure pore fluid pressure diffusion), we perform 3-D finite element numerical modeling (FEM) of the nonlinear equation of diffusion (equation(4)) with initial and boundary conditions given below. Another goal of this study is the validation of the theoretical back front scaling law derived in the previous section.

The FEM is implemented with COMSOL Multiphysics®, using an iterative **GMRES** (Generalized Minimum Residual) solver with a maximum of 50 iterations. The geometry is meshed with tetrahedral elements for the spatial discretization. The mesh is highly refined in vicinity of the injection source to resolve pressure gradients. To account for the pressure dependence of the hydraulic diffusivity $D(p)$, we apply equation (5) for different indices of nonlinearity n. Regarding the postinjection behavior of the pressure-dependent diffusivity, we apply two models. One model to consider an "elastic" behavior of the diffusivity (i.e., reversible) and another model to account for an irreversible and thus "frozen" diffusivity. These models will be discussed below.

Using the numerically derived pressure distributions in time and space, catalogs of synthetic seismicity are generated, following an approach by *Rothert and Shapiro* [2003], and spatiotemporal characteristics of synthetic triggering and back fronts are analyzed.

3.1. Numerical Solution

The numerical solution is implemented based on a hydraulic fracturing treatment in the Barnett Shale, Texas, USA (see studies by, e.g., *Hummel and Shapiro* [2012, 2013]). Here fluids have been injected through a perforated wellbore for 5.4 h with an average flow rate of 0.145 m^3/s. The average injection pressure amounted to 8.34 MPa. Both rates did vary only slightly within this interval, and pressures followed flow rate variations. During the treatment, a cumulative amount of fluid of 2683 m^3 was injected into the formation.

3.1.1. Frozen Diffusivity Model

To approximate real hydraulic fracturing and geothermal (EGS) case studies, involving propping or self-propping, respectively, assumptions about the postinjection hydraulic behavior of the medium have to be made. As the fluid injection is stopped, the pore fluid pressure p increases up to a distance-dependent maximum $p_{max}(t, r)$ and decreases thereafter. Consequently, the effective normal stress increases and previously opened fractures and cracks close. However, hydraulic fracturing of low permeable rocks is performed by the hydrocarbon industry to develop permanent flow paths for natural oil and gas. Therefore, proppants are added to the fracturing fluid [*Mader*, 1989]. These small particles prevent the pore space from closing and maintain the desired flow paths. A similar effect can be achieved in some cases by a self-propping shear dilatation at EGS [*Durham and Bonner*, 1994]. To account for this postinjection hydraulic behavior of the medium, *Hummel and Shapiro* [2016] proposed the following frozen diffusivity model.

Terminating the fluid injection at t_0 leads to the relaxation of pore fluid pressure in the form of a diffusional wave with a pressure maximum $p_{max}(t, r)$ at $r = \sqrt{x^2 + y^2 + z^2}$. As soon as the pressure maximum is reached after the injection stop, the pressure decreases. If the diffusivity D is a function of pressure, it will behave similar to the pressure perturbation. It increases up to a distance-dependent value $D_{max}(p_{max}(t, r))$ and would decrease thereafter. However, added proppants preserve the enhanced diffusivity. Therefore, the frozen diffusivity model keeps the diffusivity at each location in the model constant at $D(p(t, r)) = D_{max}(p_{max}(t, r))$ as soon as the pressure decreases.

3.1.2. Elastic Diffusivity Model

In addition to the frozen diffusivity model, we test a nonlinear model considering a reversible elastic behavior of the hydraulic diffusivity. In this model, the previously enhanced medium diffusivity $D(p)$ is not held constant but is allowed to decrease as soon as the pore fluid pressure has reached its local maximum $p_{max}(t, r)$.

Note that a real behavior of the diffusivity will be between these two asymptotic situations, the frozen diffusivity model and the elastic diffusivity model.

3.1.3. Model Geometry, Governing Equations, and Boundary Conditions

For our numerical model, the stimulated rock volume is represented by a sphere with the radius $r_R = 500$ m. This is large enough to exclude any significant numerical interaction between the outer boundary of the model and the pressure perturbation. Following previous works [see, e.g., *Dinske*, 2010; *Hummel*, 2013], real fluid injection scenarios, where fluids are injected through an open hole or a perforated interval of the wellbore, can be approximated by an effective injection source cavity. Thus, the injection source in our model is realized by a smaller sphere of the radius $r_S = 0.5$ m (as defined by *Hummel* [2013]), located in the center of the large sphere. We do not include actual fractures in our scenario, but the pressure is only allowed to diffuse from the injection source into the spherical model space. Such a geometry effectively approximates the complex 3-D geometry of a hydraulic fracturing treatment which strongly interacts with a 3-D network of preexisting cracks, as observed, for example, in the Barnett Shale [*Hummel and Shapiro*, 2013] (see also Figure 1).

We assume an isotropic pressure-dependent diffusivity $D = D(p(t, r))$ which follows a power law dependence on pressure (equation (5)). For the postinjection interval, the two aforementioned models of diffusivities are applied. To solve for the equation of nonlinear diffusion (equation (4)), we use nonlinearity indices $n = 1, 2, \ldots, 5$.

In our modeling procedure, the scaling parameter D_0 is adjusted for each value of n such that the pore fluid pressure $p(x, y, z, t_0)$ at $t = t_0$ does not penetrate beyond a radial distance of $r_{\max,t_0} = 250$ m from the injection point. This maximum penetration distance is taken from the farthest triggered event distance from the source of a typical case study like, e.g., the Barnett Shale seismicity [*Hummel*, 2013].

Initial pressures in the model area are set to $p(x, y, z, t < 0) = 0$ Pa. The fluid injection is realized by a Dirichlet-type boundary condition with $p = p_0$. For this, a boxcar-like injection pressure with a duration of $t_0 = 5.4$ h is defined on the surface of the source cavity. It is switched on at $t = 0$ h and has a magnitude of $p_0 \approx 8.34$ MPa. After the injection stop at $t = t_0$, the pressure at the source is set to 0 Pa. The boundary condition at the outer edge of the model at a large $r = r_R = 500$ m is represented by $\frac{\partial p}{\partial t} = 0$ for the whole modeling time, i.e., by a no-flow boundary.

The time interval of the study is set to $t = [0\text{ h}, 11.1\text{ h}]$ with time increments of $\Delta t = 60$ s.

3.2. Synthetic Seismicity

In the following, pressure distributions obtained from both models are used for the generation of catalogs of synthetic seismicity. For this, we apply a method introduced by *Rothert and Shapiro* [2003]. It is based on the hypothesis that rocks contain preexisting fractures and cracks which are critically stressed. Therefore, even small perturbations of pore fluid pressure p above the in situ pore fluid pressure level can modify the effective normal stress such that seismic events are induced. This observation leads to the following triggering criterion:

$$p(x, y, z, t) > C(x, y, z)\,. \tag{27}$$

It results from the classical Mohr-Coulomb failure criterion, i.e., shear failure of optimally oriented faults, and states that a seismic event is triggered, if the pore fluid pressure $p(x, y, z, t)$ exceeds the critical value $C(x, y, z)$ at a certain location (x, y, z) at a given time t. C is a function of in situ stresses and friction along planes of weakness, and values correspond to pressures necessary for shear failure and sliding along preexisting, optimally oriented critically stressed cracks and fractures.

Assuming that a number of randomly generated critical values $C(x, y, z)$ are equally distributed between a minimum value $C_{\min}$ and a maximum of $C_{\max}$, the criticality field C is defined. For our modeling, the minimum is set to $C_{\min} = 10^5$ Pa. According to *Rothert and Shapiro* [2007], this is a representative value. The maximum value $C_{\max}$ is given by the injection pressure (i.e., $C_{\max} \approx 9$ MPa), which is the highest pore fluid pressure value that can induce an event, considering the triggering criterion equation (27). A maximum value is required to get an integral of 1 for the probability density function of C. Physically, this value sets a limit to the distribution of critical pressure values.

Possible hypocenter locations are defined by a grid of random, uniformly distributed points (X, Y, Z) within a sphere [*Knuth*, 1998]. In the following, each value of C, being random within $[C_{\min}, C_{\max}]$, is assigned with one location such that $C = C(X, Y, Z)$. Furthermore, numerically obtained pore fluid pressures $p(x, y, z, t)$ are interpolated on the locations (X, Y, Z) such that $p(x, y, z, t) = p(X, Y, Z)$.

The triggering is confined such that once a seismic event is triggered at a certain location (X, Y, Z), the local criticality is set to a value higher than expected from the pressure distribution. This restriction prevents multiple triggering at one specific location to exclude healing of fractures and cracks due to tectonic loading, which would take much longer compared to the modeling time.

3.3. Fitting Algorithm and Error Estimates

For the fit of equations (6) and (7) to the seismic clouds, event distances $r = \sqrt{x^2 + y^2 + z^2}$ from the source are plotted versus their occurrence times t, yielding r-t plots.

To get an estimate of the triggering front, we look for the farthest triggered events (FEs) at each time step t_i during the injection first. The algorithm works as follows: the first event induced at time step t_i with $i = 1$ is taken as a starting point, i.e., the first FE. The algorithm then checks the event distances at the subsequent time step t_{i+1}. If the event with the largest distance at this time step occurred farther away from the source than the previous FE, this event is registered as the second FE and is taken as the starting point for the next iteration. If no event distance was larger than that of the previous FE, the algorithm proceeds to the next time step t_{i+2} and checks the event distances for this time. As soon as an FE is found, it is taken as a starting point for the next iteration. This procedure is repeated until the injection stop time t_0 is reached and then continued for events after the injection stop.

Regarding the back front of seismicity, the algorithm works similar to the one described above for triggering front events. However, it starts with the back front event (BFE) induced at the last time step t_n and looks regressively for induced events that are closer to the source in previous time steps t_{n-1} until the injection stop at $t = t_0$.

Subsequently, we perform a nonlinear regression to fit power law functions to determine triggering and back fronts (equations (6) and (7)). For this, we use the nonlinear optimization tool "fminsearch" in MATLAB®. This tool aims at finding a local minimum of the power law functions, equations (6) and (7), using the so-called Nelder-Mead simplex algorithm as described by *Lagarias et al.* [1998].

We note that synthetic seismic clouds are influenced by numerical errors caused by the chosen mesh size and applied time stepping. To minimize errors caused by the mesh, an adaptive mesh refinement was implemented. Yet inaccuracies in the pressure distribution cannot be excluded. Further, synthetic event locations are subject to the triggering and fitting algorithms. In contrast, recorded seismic event locations are biased by mislocalization, which affects especially events in vicinity of the injection source. Additionally, there is often a lack of event recordings in the postinjection time.

To account for these errors, we apply 95% confidence intervals (CIs) to the curves fitted to the determined FE and BFE. Thus, we assume that the assigned values of A, χ, B, and ψ are statistically significant within the 95% CI, concluding that the obtained values are reasonable estimates accounting for different sources of errors. For this, the MATLAB® nonlinear regression function "nlfit" is applied with starting values returned by fminsearch. The output obtained by this is then used together with the functions "nlparci" and "nlpredci" to get confidence and prediction intervals for the fitting parameters A, B, and χ, ψ.

3.4. Discussion of Numerical Results

From the numerical modeling we obtain pore fluid pressure distributions $p(x, y, z, t)$ as well as distributions of the diffusivity $D(x, y, z, t) = (n + 1)D_0 p^n$. Figure 3 (left column) shows pore fluid pressure profiles taken along the radial distance r from the injection point for different times (color-coded) and for both model realizations. Solid lines indicate results obtained from the frozen diffusivity model, dashed lines represent values derived from the reversible elastic model. The results are shown for indices of nonlinearity $n = 1, 3, 5$ (top to bottom), where $n = 1$ indicates only slight nonlinear diffusion and $n = 5$ represents a case of rather strong nonlinearity.

Noticeable is the distinct pressure decrease in the vicinity of the source, which is analogous to the observation of geometrical spreading in the case of classical propagating waves. The nonlinearity of the pressure diffusion impacts on the shape of the profiles as well as on the pressure magnitude. Increasing nonlinearity leads to more pronounced piston-shaped profiles defined by a distinct pressure drop to zero at the tip of the profile. Furthermore, the stronger the nonlinear fluid-rock interaction, the higher the corresponding pressure values along the profile.

Concentrating on the postinjection phase, the influence of the diffusional-like wave becomes evident. As a result of the termination of the fluid injection at $t = t_0 = 5.4$ h, the pressure defined on the surface of

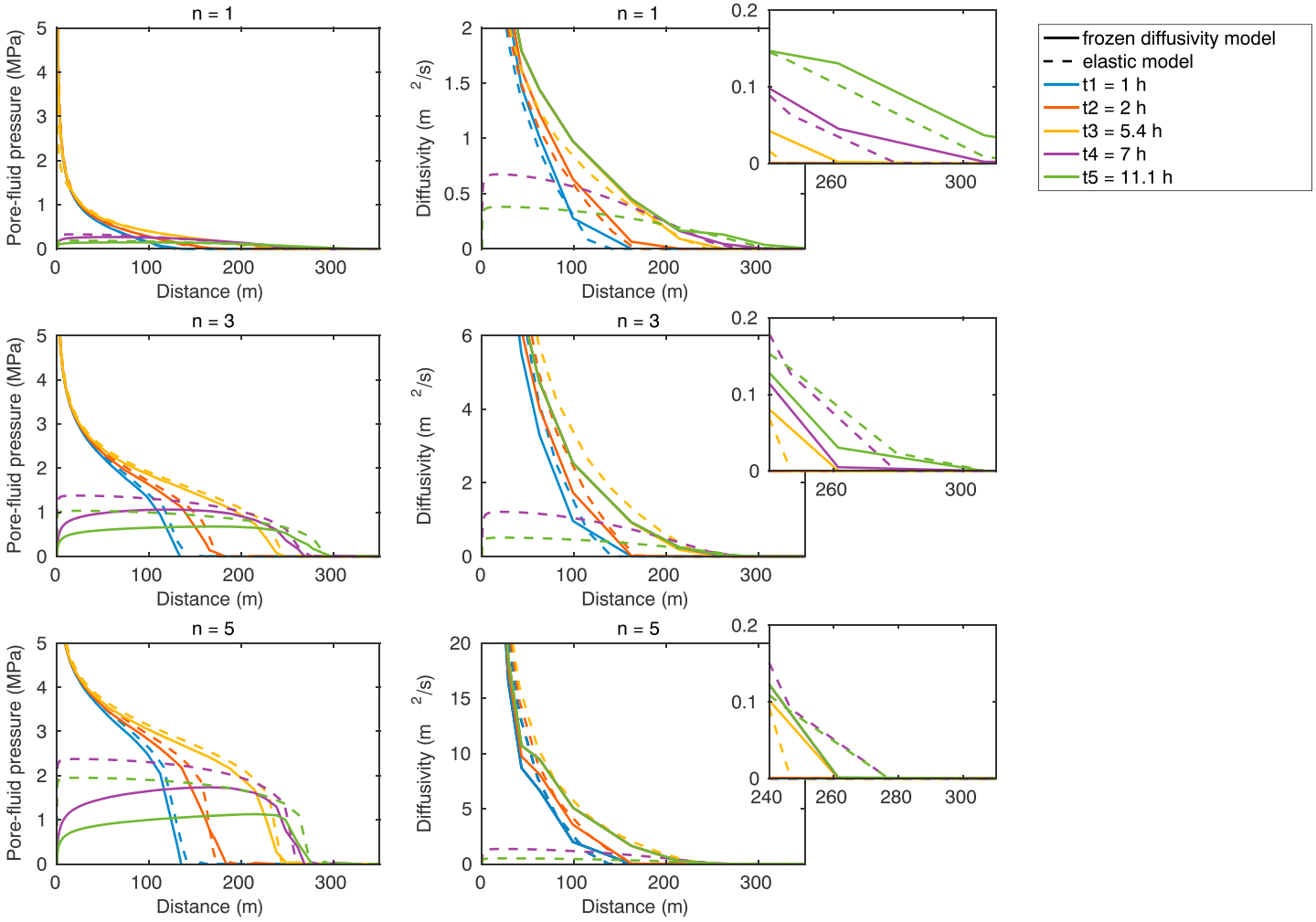

Figure 3. (left column) Numerically derived pore fluid pressure distributions in time and space for different indices of nonlinearity, plotted as pressure profiles for different time steps. A distinct pressure drop characterizes the pressure evolution in vicinity of the borehole as well as the tip of the profiles. The higher the nonlinearity, the more pronounced the piston shape of the profiles. Remarkable differences between both models develop after the injection stop at $t_0 = 5.4$ h. This observation is caused by different realizations of the behavior of the pressure-dependent hydraulic diffusivity $D(p)$. (right column) The evolution of the pressure-dependent diffusivity $D(p)$, obtained from equation (5). Until the injection stop at $t = 5.4$ h (yellow line), the diffusivity for both models varies only slightly. As soon as the pressure drops to 0 Pa, the diffusivity of the "elastic" model follows the pressure evolution, whereas the $D(p)$ in the frozen model remains at its local maximum value.

the source decreases to zero. Nonetheless, the diffusional wave of pore fluid pressure still penetrates farther into the medium. It increases slowly with distance up to a certain pressure maximum $p_{max}(t > t_0, r)$. This maximum $p_{max}(t > t_0, r)$ depends on the index of nonlinearity as well as on the distance from the source. The higher the index on nonlinearity and the smaller the distance from the source, the higher the maximum value. Additionally, stronger fluid-rock interaction leads to earlier pressure maxima. However, as soon as the maximum is reached, pressure starts to decrease, marked by a pressure drop at the tip.

Regarding the course of the pressure-dependent diffusivity $D(p)$ given by equation (5), distinct differences between the frozen and elastic diffusivity models can be observed after the injection stop at $t = 5.4$ h. During the injection (at times $t < 5.4$ h), the diffusivity follows the pressure evolution, which is almost the same for both models. However, as soon as the injection pressure is set to 0 Pa at $t = 5.4$ h, the diffusivity in the elastic model drops to zero at the source and increases only slightly further within the medium. In contrast, the diffusivity in the frozen diffusivity model does not decrease after $t = 5.4$ h. Rather, it is held constant at its local value as soon as the pressure starts to decrease at this location. Consequently, the diffusivity in this model

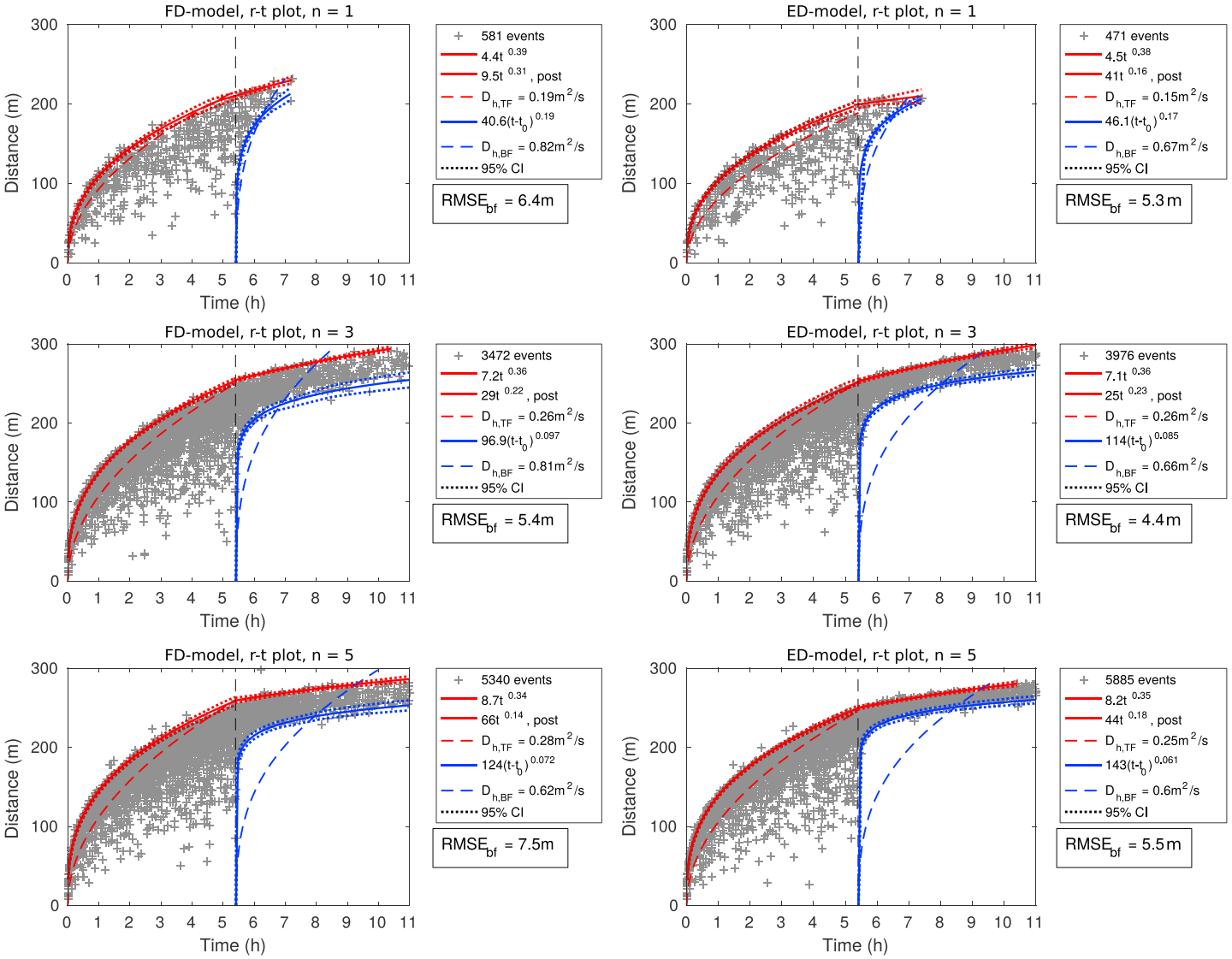

Figure 4. *r-t* plots of synthetic events generated from pressure distributions (left column) of the frozen diffusivity model and (right column) of the reversible elastic realization for different indices of *n*. Regarding spatiotemporal characteristics, the nonlinearity of the diffusion is indicated by a rather cubic root of time-dependent triggering front and an exponent of $\psi < 1/3$ for the back front. Differences between the *r-t* plots of both models, especially after the injection stop (black, dashed line), are related to different pressure distributions. Thin, dotted lines mark the confidence interval of the fit of 95%. The root-mean-square error (RMSE) for the nonlinear regression of the back front of all model realizations <10 m which is smaller than localization errors of real data.

increases after the injection stop only at larger distances. Regardless of the model, the diffusivity increases with higher nonlinearity *n* by more than 1 order of magnitude from more than 6 m^2/s at $n = 1$ to over 60 m^2/s at $n = 5$.

The spatiotemporal evolution of pore fluid pressure derived from the numerical modeling leads to characteristic seismic clouds. Spatiotemporal event distributions are shown in Figure 4 for $n = 1, 3, 5$ (top to bottom) for the frozen diffusivity model (left column) and for the reversible elastic realization (right column).

Focusing on the injection phase, the evolution of the seismicity for both models coincides. The seismic clouds are characterized by a sharp upper boundary with a concentration of events. This front is also known as the triggering front and describes the distance beyond which the medium has not yet been pressurized. A square root fit according to equation (2) to the farthest triggered events (FEs) in both models, which were found as described above, does not represent spatiotemporal signatures very well (dashed red lines). Fitting equation (6) to the FE, using the algorithm outlined in the previous chapter, confirms that the temporal behavior of the triggering front does not correspond to a $\sqrt{t}$ dependence but shows nearly cubic root signatures

Table 1. Values of the Exponent ψ (Equation (7)) Obtained From Synthetic Data and Real Data Examples From Literature[a]

FD Model	Observed ψ	Predicted $1/(dn+2)$	ED Model	Observed ψ	Predicted $1/(dn+2)$
$n=1$	$0.17 < 0.19 < 0.21$	0.20	$n=1$	$0.15 < 0.17 < 0.19$	0.20
$n=2$	$0.11 < 0.13 < 0.14$	0.125	$n=2$	$0.11 < 0.12 < 0.13$	0.125
$n=3$	$0.085 < 0.097 < 0.11$	0.091	$n=3$	$0.079 < 0.086 < 0.092$	0.091
$n=4$	$0.081 < 0.089 < 0.098$	0.071	$n=4$	$0.062 < 0.068 < 0.073$	0.071
$n=5$	$0.063 < 0.072 < 0.082$	0.059	$n=5$	$0.053 < 0.061 < 0.068$	0.059
Hydraulic fracturing data				observed ψ	estimated n
Horn River Basin (relocated events by A. Reshetnikov)				$0.095 < 0.16 < 0.22$	$2.5 < 4.3 < 8.6$
Montney Shale, lower (r-t by *Birkelo et al.* [2012])				0.14	5.1
EGS data				observed ψ	estimated n
Basel 2006				$0.11 < 0.21 < 0.30$	$0.45 < 0.95 < 2.3$
Cooper Basin 2003				$0.11 < 0.18 < 0.25$	$0.69 < 1.2 < 2.5$
Fenton Hill (ψ by *Hummel and Shapiro* [2016])				0.33	0.34
Ogachi (ψ by *Hummel and Shapiro* [2016])				0.36	0.26

[a]For synthetic data, also predicted values for $1/(dn+2)$ (equation (25)) are given for the frozen diffusivity model (FD model) and the reversible elastic diffusivity model (ED model). For real data, equation (25) was applied, yielding estimates of the nonlinearity n within 95% confidence intervals. Values of observed ψ and predicted $1/(dn+2)$ are plotted in Figure 5.

(solid red lines). This characteristic is found for both models and indicates nonlinear diffusion of pore fluid pressure. For the elastic diffusivity model (ED model), the fit yields exponents χ between 0.38 and 0.35 for $n=1$ and $n=5$, respectively. In comparison, for the frozen diffusivity model (FD model), values of χ between 0.39 and 0.34 for $n=1$ and $n=5$, respectively, are obtained. The 95% CI is marked by thin, dotted red lines.

In terms of postinjection-induced seismicity, the triggering front seems to change its temporal evolution. Events occur at smaller distances than predicted by the triggering front from equation (6). Values of χ derived from the fit of equation (6) to farthest triggered events after the injection stop get smaller for the postinjection triggering front (solid red lines, indicated in the respective legend by "post"). This observation corresponds to the derived scaling law for the triggering front at times $t > t_0$ (equation (26)). Furthermore, seismic event clouds for both models reveal a domain of seismic quiescence which evolves with time $t > t_0$ from the injection source. A linear diffusion back front according to equation (3) does not adequately describe the temporal behavior of postinjection-induced seismicity (dashed blue lines). Therefore, equation (7) is applied to synthetic seismicity for both models (solid blue lines), using the fitting algorithm (explained above). Values of ψ are summarized in Table 1. For the FD-model, this yields exponents between 0.19 and 0.072 for $n=1$ and $n=5$, respectively. In comparison, values decrease from 0.17 to 0.061 between $n=1$ and $n=5$ for the reversible elastic model. For both models $\psi < 1/3$, which again is typical for seismicity induced by nonlinear diffusion. The 95% CI of the back front fit is marked by thin blue lines. For all model realizations, the front lies well within this interval. Root-mean-square errors (RMSE) of the estimated front obtained from the nonlinear regression are given in each subfigure. Values are <10 m. This is smaller than typical localization inaccuracies of data, which are usually in the range of tens of meters. Thus, the determined back fronts can be assumed to be a good approximation of the spatiotemporal evolution of microseismic events.

4. Validation of the Scaling and Application to Real Data

The novel scaling law for the back front of seismicity (equation (25)) demonstrates that the temporal behavior of the back front of seismicity is consistent with the idea that the back front of seismicity is controlled by the nonlinearity of pore fluid pressure diffusion and the Euclidean dimension of the dominant growth of the seismic cloud. To validate this finding, we compare the theoretical exponent $1/(dn+2)$ to the exponent ψ, which was obtained from a power law fit to synthetic seismicity (equation (7)). Subsequently, we apply the scaling to real data examples. Observed values of ψ, predicted values of $\psi = 1/(dn+2)$ for the synthetic data, and estimates of n for real data are also summarized in Table 1.

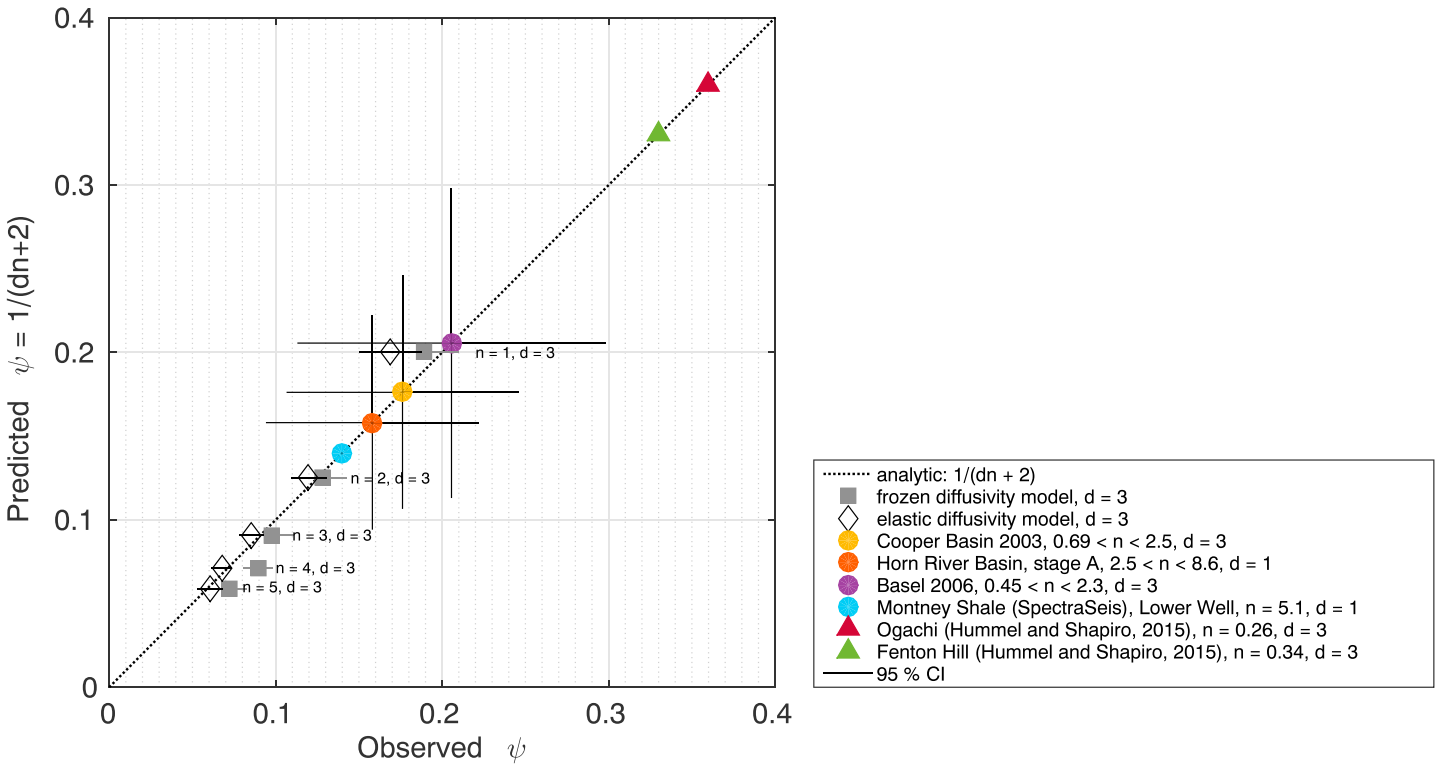

Figure 5. Theoretical relation for the back front scaling compared to exponents ψ derived for the frozen diffusivity and elastic model as well as to observed real data examples. The values of ψ derived for the synthetic seismicity as well as for real data examples coincide with theoretically predicted values from equation (25). Thin solid lines show the 95% confidence interval of the fitted parameter ψ.

In Figure 5, predicted values of the theoretical exponent $1/(dn + 2)$ are plotted versus observed values of ψ, including error bars. Focusing on the synthetic seismicity, the derived exponents are well approximated by the theoretical line. This is especially the case for synthetic seismicity for the reversible elastic model. Slight discrepancies between the theoretical value and ψ derived for the frozen diffusivity model are attributable to the fact that equation (25) does not describe a frozen diffusivity. Despite this, it can be concluded that the derived scaling law can explain the controlling parameters of the back front which evolves after the termination of a fluid injection. Thus, the relation can be used for parameter estimates if one of the parameters is unknown.

For a demonstration of this advantage, we apply the $\psi = 1/(dn + 2)$ dependence to real data examples. Note that fluid-induced seismicity frequently occurs in hydraulically anisotropic media. To account for this anisotropy, we use an effective isotropic medium transformation introduced by *Hummel* [2013] for seismic clouds induced at the Basel and Cooper Basin EGS sites before a fit of both fronts.

Case studies from hydraulic fracturing operations performed by the hydrocarbon industry in Canada, Horn River Basin and Montney Shale [see, respectively, *Baig et al.*, 2015; *Birkelo et al.*, 2012], are two examples where the Euclidean dimension of the seismic cloud can be estimated from the dominant growth tendency of the microseismic cloud, yielding $d = 1$. Such a one-dimensional case, depicted in Figure 1a, indicates that seismic events occur on or at least close to the created classical hydraulic fracture such that their locations can be projected onto the fracture. Since the equation of diffusion (equation (4)) we solved numerically (section 3.1) is also valid for 1-D scenarios, the theoretical scaling law can be applied here. Now we have a chance to estimate the strength of nonlinear pore fluid pressure diffusion. Fitting function (7) to the back front in corresponding *r-t* plots (solid blue lines in Figures 6 and 7) yields exponents ψ. For the Horn River Basin it is $\psi_{HRB} = 0.16$ (solid blue line) within a CI of $\psi = [0.095, 0.22]$ (dotted blue lines). This rather large interval for ψ results from a lack of events after the injection stop, which makes a definition of the back front difficult. Regarding the Montney Shale case, a fit to the lower well induced seismicity results in $\psi_{Mo} = 0.14$. The application of CI was not possible in this case, since the fit was implemented only for the *r-t* plot by *Birkelo et al.* [2012] without exact

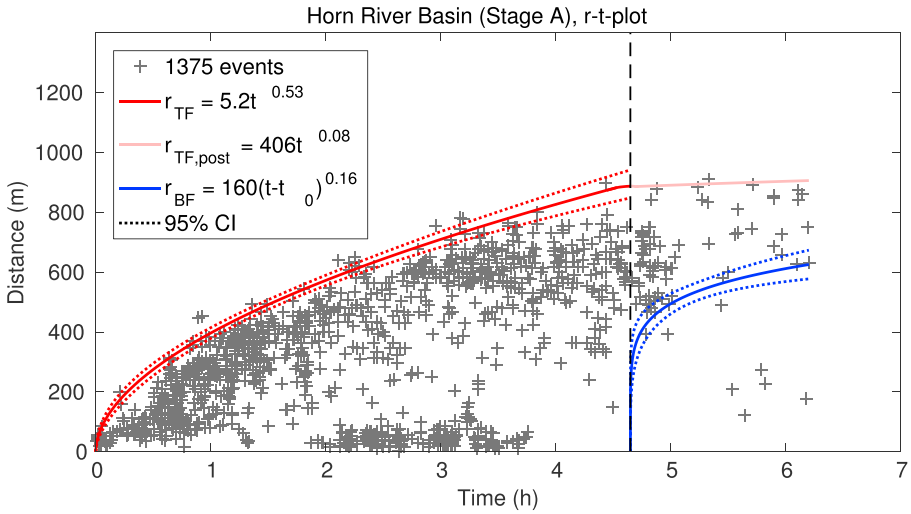

Figure 6. *r-t* plot of Horn River Basin seismicity. Seismicity induced by the fluid injection can be related to nonlinear diffusion, indicated by a temporal dependence with $\chi < 1/2$ for the triggering front and with $\psi = 0.16$ for the back front. After the injection stop (black, dashed line), the triggering front clearly changes its behavior as predicted by equation (26). Note that $\chi \approx 1/2$ of the triggering front for the case of a nearly 1-D hydraulic fracture is an indication of strong leak-off into the surrounding reservoir [see *Shapiro*, 2015, chap. 4]. Dotted lines indicate the 95% confidence interval. Data have been provided by a sponsor of the *PHASE* consortium. We thank A. Reshetnikov for relocating the events.

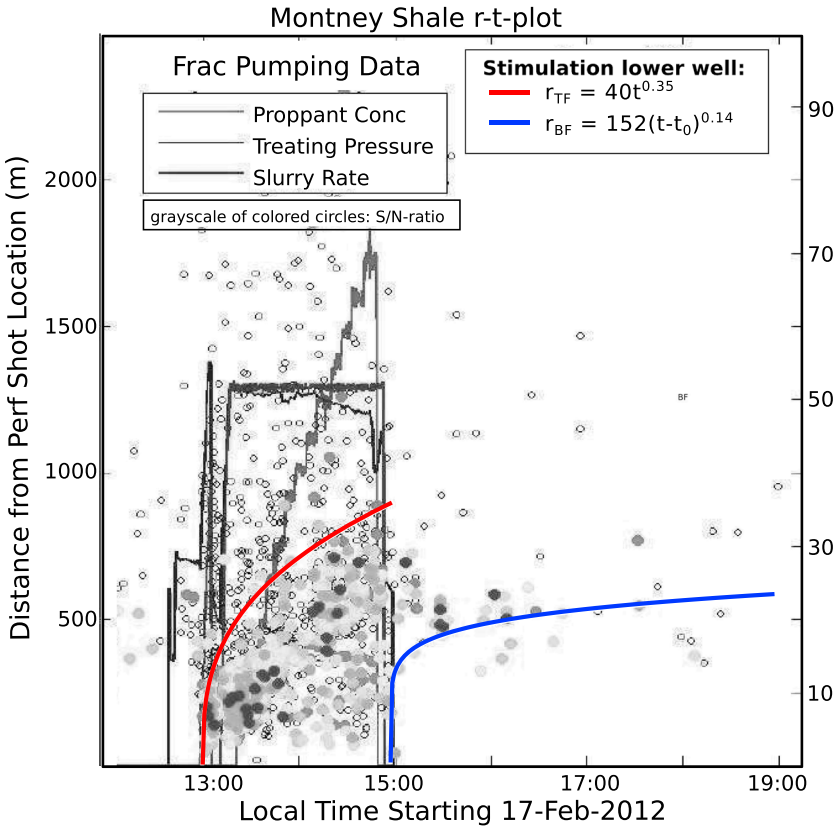

Figure 7. Stimulation of two different wells in the Montney Shale led to fluid-induced seismicity. The spatiotemporal event distribution indicates that seismicity in the Lower Montney Shale was induced by nonlinear pore fluid pressure diffusion. The injection was stopped at approximately 15:00. *r-t* plot by *Birkelo et al.* [2012].

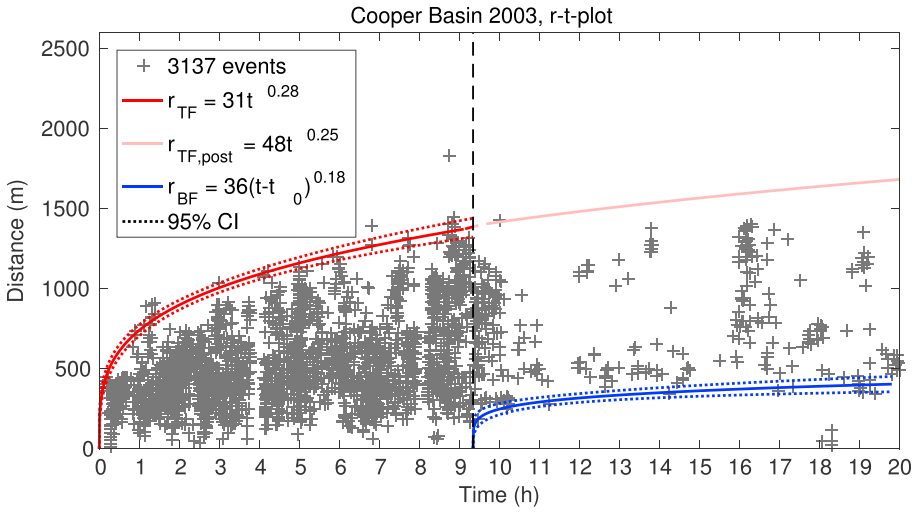

Figure 8. Cooper Basin *r-t* plot of events in an effective isotropic medium. Power law fits to the triggering front and the back front of seismicity with equations (6) and (7) reveal that seismicity was induced by nonlinear diffusion of pore fluid pressure. As soon as the injection pressure at the source ceases (indicated by the black, dashed line), the slope of the triggering front changes which is in accordance to the scaling law for the triggering front after the injection stop (equation (26)). Dotted lines mark the confidence interval of 95% of the fit. The data are courtesy of H. Kaieda. [see also *Shapiro and Dinske*, 2009].

event locations. Thus, the errors can be assumed to be rather large. To determine the strength of influence of nonlinear pore fluid pressure diffusion for both case studies, observed values of ψ are plotted in Figure 5. For the Horn River Basin stimulation, also error bars resulting from the 95% confidence interval are shown. Given that the diffusion of pore fluid pressure in both cases occurred along a 1-D hydraulic fracture (i.e., $d = 1$) and using the obtained value of ψ, a best fit to the theoretical law for the Horn River Basin is achieved for $n = 4.3$, which lies within the 95% confidence interval of $n = [2.5, 8.6]$. For the Montney Shale, n is determined to be $n = 5.1$ for the lower well hydraulic fracturing treatment.

Two case studies from EGS operations in Basel, Switzerland, and Cooper Basin, Australia, further confirm the applicability and advantage of the scaling law [see *Häring et al.*, 2008; *Asanuma et al.*, 2005]. Again, function (7)

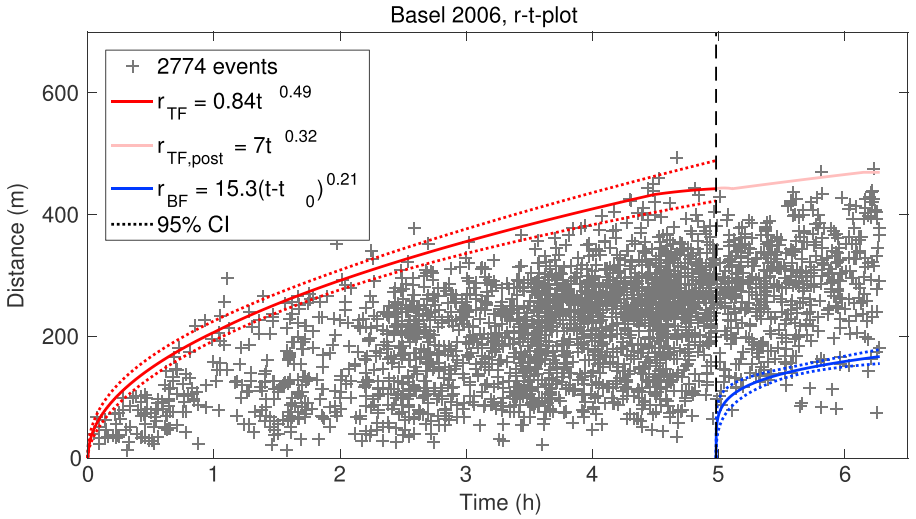

Figure 9. *r-t* plot of seismicity in an effective isotropic medium at the EGS site Basel. Seismicity induced by the fluid treatment is assumed to be related to a slightly nonlinear diffusion of pore fluid pressure as indicated by $\psi < 0.3$ for the back front. The triggering front clearly changes its temporal behavior after the injection stop (black, dashed line). Dotted lines indicate the 95% confidence interval of the fit. The data are courtesy of U. Schanz and M. O. Häring [see also *Shapiro and Dinske*, 2009].

can be fitted to seismic back fronts in corresponding *r-t* plots with a confidence interval of 95% (see Figures 8 and 9, solid and dotted blue lines, respectively). This gives exponents ψ for both reservoirs with $\psi_{Ba} = 0.21$ in an interval of $\psi = [0.11, 0.30]$ and $\psi_{CB} = 0.18$ between $\psi = [0.11, 0.25]$. In both cases, hydraulic fracturing operations induced 3-D seismic clouds. Therefore, plotting observed values of ψ in Figure 5 and assuming $d = 3$, the influence of nonlinear fluid-rock interaction can be estimated. Obviously, seismicity in the Basel EGS operation was controlled by only weak nonlinear diffusion of pore fluid pressure, $n = 0.95$ within boundaries of $0.45 < n < 2.3$. In the Cooper Basin, nonlinear pore fluid pressure diffusion was slightly higher, yielding $n = 1.2$ with lower and upper boundaries of $0.69 < n < 2.5$. The difference between the two scenarios may be related to different in situ stress regimes: Whereas the stress field at the Basel EGS site can be characterized by a strike-slip regime [*Kraft and Deichmann*, 2014], maximum principal stresses are horizontal at Cooper Basin, indicating a thrust fault regime [*Baisch and Vörös*, 2010].

Comparing the case studies for EGS operations and hydraulic fracturing of hydrocarbon reservoirs, a distinct difference of *n* can be seen. The influence of nonlinear diffusion at the examined hydraulic fracturing sites Montney Shale and Horn River Basin is much larger than that observed during EGS operations in Basel and Cooper Basin. Such an observation correlates well with the actual aim of hydraulic fracturing of hydrocarbon reservoirs and the hydraulic stimulation of geothermal sites: Injection pressures usually do not exceed the local minimum stress at EGS (see, e.g., for Basel) [*Häring et al.*, 2008], which prevents the opening of new fractures. In contrast, the production of unconventional hydrocarbons from tight formations requires massive fracturing of the rock by injection pressures higher than the minimum in situ principal stress. Such a process may artificially increase the in situ hydraulic diffusivity and permeability by several orders of magnitude [see *Shapiro*, 2015, p. 200], resulting in nonlinear diffusion as discussed above.

5. Discussion of Assumptions and Competing Models

Recently, several models have been developed to describe spatiotemporal characteristics of fluid-induced seismicity during as well as after the injection.

Among these models, poroelastic coupling models were developed to describe injection- and production-induced seismicity. (as discussed by, e.g., *Rutqvist et al.* [2008], *Rozhko* [2010], *Segall and Lu* [2015], and *Chang and Segall* [2016]). These works are all based on Biot's idea [*Biot*, 1941] that pressure changes, such as caused by fluid injections, induce a stress field. In turn, these stresses might affect pore fluid pressures. For more information, see also section 1.

Yet for the case of injections into low permeable rocks, the observed spatiotemporal distribution of microseismic events induced by proppant injections or self-propping processes is adequately described by incorporating only pore fluid pressure diffusion, while ignoring poroelastic fluid-to-solid coupling [see, e.g., *Talwani and Acree*, 1984; *Shapiro et al.*, 1997, 1999, 2002]. Also, we note that a diffusion model is the end-member case of poroelastic coupling in which the poroelastic coupling parameter $\alpha \rightarrow 0$. Therefore, such a scenario is an important and necessary step for further understanding of seismicity-controlling mechanisms.

For the purpose of the derivation of the novel scaling relation as described above, we accepted nonlinear diffusion of pore fluid pressure, in which the hydraulic diffusivity becomes a function of pressure as the driving force behind observed seismic events. This process was studied in detail by *Shapiro and Dinske* [2009] and further described, e.g., by *Hummel and Shapiro* [2013] and *Shapiro* [2015]. Other nonlinear diffusion models were, for example, developed and adapted by *Rice* [1992], *Miller et al.* [2004], *Gischig and Wiemer* [2013], and *Miller* [2015].

Certainly, a model of nonlinear pore fluid pressure diffusion is just one mechanism to describe real observations of injection-induced seismicity. Other models, which additionally include stress changes related to the seismicity rate, as proposed by *Dieterich* [1994] and applied by *Segall and Lu* [2015], might also be a contributing explanation for injection-induced seismic events.

We do not want to exclude other possible seismicity-controlling mechanisms. However, the application and combination of many different factors is beyond the scope of the work presented in this paper, which aimed at the derivation of a novel scaling relation to explain observed features of postinjection-induced seismicity. Our approach showed that a rather straightforward model can explain observed microseismic features; that is, microseismicity after the injection stop is mainly controlled by the nonlinearity of the diffusion process as

well as the dimension of the dominant growth direction of the seismic cloud. Nonetheless, it is already under consideration to include poroelastic pressure-stress coupling to future nonlinear diffusion models.

We studied a simplified case of equally distributed possible hypocenter locations with a uniform distribution of critical pressure values. It is likely that large faults exist in the medium which might act as possible fast pathways for the pressure or for stress transmission to deeper levels [*Chang and Segall*, 2016]. Furthermore, in situ stresses might have a significant impact on the evolution of seismic hypocenter locations. Therefore, for explicit case studies in future, knowledge of preexisting fractures as well as the in situ stress regime should be included in the model.

Regarding possible leak-off effects caused by fluids which enter the formation from the hydraulic fracture, we can qualitatively state the following: Our model implies that the leak-off is significant for small n ($n \leq 1$) but vanishes if n is significantly higher than 1. With respect to flowback volumes, for negligible leak-off ($n > 1$) and the elastic model, flowback will be approximately equal to the injected volume. In the frozen model, flowback will be significantly smaller. In the case of a high leak-off ($n < 1$), the flowback to the borehole will vanish. Note that a high n just means a volume balance: The volume of the opened pore space is approximately equal to the injected fluid amount.

Assuming that fluid-induced seismicity is controlled by a rather general case of pore fluid pressure diffusion, we fitted power law functions to the triggering and back front of seismic clouds. This yields estimates of the temporal dependence, given by exponents ψ. In order to account for numerical errors as well as inaccuracies caused by triggering and fitting algorithms for synthetic data and localization uncertainties as well as rare postinjection-induced events of real data, we introduced 95% confidence intervals of the triggering and back front fits, which are an accepted measure for inaccuracies in statistics. Corresponding *r-t* plots illustrate that these intervals are a good approximation. Regarding the application of the scaling law (equation (25)) to real observed data, the significance of 95% results in a range of values for the index of nonlinearity n. This uncertainty has to be considered when the values are used for further reservoir simulations and hazard assessments.

6. Conclusion

For the numerical 3-D solution of nonlinear pore fluid pressure diffusion, we assumed a power law dependence of the hydraulic diffusivity on pressure [*Shapiro and Dinske*, 2009]. We applied two different models regarding postinjection behavior of the hydraulic diffusivity, a frozen diffusivity model as introduced by *Hummel and Shapiro* [2016] and a reversible elastic model. Even if the latter one is easier to implement, the frozen diffusivity model captures the usage of proppants added to the fracturing fluid to keep the hydraulic diffusivity constant after the injection stop. Nevertheless, real configurations are somewhere between these to end-member approximations, explaining the implementation of both models, the frozen diffusivity model and the reversible elastic model.

We proposed a novel scaling law for the back front of induced seismicity. It reveals that postinjection-induced seismicity is sensitive to the nonlinearity (quantified by the index n) of the diffusion process and to the Euclidean dimension d of the preferential direction of growth of the seismic cloud. Therefore, the derived dependence becomes of particular importance when one of the two parameters is unknown. This may be fundamental for the development and the optimization of hydrocarbon reservoirs, for example, for modeling of production. The validity of the theoretical dependence was verified by synthetic data and was subsequently successfully applied to data from case studies.

Seismic monitoring systems and long-enough record times after the termination of the fluid injection are crucial for successful and reliable assessments of the controlling hydraulic parameters and thus for the optimization of production of hydrocarbons from unconventional reservoirs (or operation of EGS sites) and seismic hazard assessment.

Acknowledgments

We thank the sponsors of the *PHASE* consortium project for supporting the research presented in this manuscript. Microseismic data used for this work have been provided by sponsors of the *PHASE* consortium project and cannot be made publicly available. However, the data are properly cited and referred to in Table 1 and in the reference list. Corresponding *r-t* plots are visualized in the manuscript. Numerical data, MATLAB codes, and synthetic seismicity can be obtained upon request from the authors (lisajohann@zedat.fu-berlin.de). The data are visualized in the corresponding figures and are also listed in Table 1. We thank the Associate Editor Doug Schmitt, the reviewer Adam Baig, and one anonymous reviewer for their helpful and constructive comments which substantially improved the quality of the manuscript.

References

Al-Wardy, W., and R. W. Zimmerman (2004), Effective stress law for the permeability of clay-rich sandstones, *J. Geophys. Res.*, *109*, B04203, doi:10.1029/2003JB002836.

Asanuma, H., N. Soma, H. Kaieda, Y. Kumano, T. Izumi, K. Tezuka, H. Niitsuma, and D. Wyborn (2005), Microseismic monitoring of hydraulic stimulation at the Australian HDR project in Cooper Basin, paper presented at World Geothermal Congress 2005, Antalya, Turkey, 24–29 Apr.

Baig, A., G. Viegas, T. Urbancic, E. v. Lunen, and J. Hendrick (2015), To frac or not to frac: Assessing potential damage as related to hydraulic fracture induced seismicity, *First Break*, *33*(7), 67–71.
Baisch, S., and R. Vörös (2010), Reservoir induced seismicity: Where, when, why, how strong?, paper presented at World Geothermal Congress, 2010, Bali, Indonesia, 25–29 Apr.
Barenblatt, G. I. (1996), *Scaling, Self-Similarity and Intermediate Asymptotics*, Cambridge Univ. Press, New York.
Berryman, J. G. (1992), Effective stress for transport properties of inhomogeneous porous rock, *J. Geophys. Res.*, *97*, 17,409–17,424, doi:10.1029/92JB01593.
Biot, M. (1941), General theory of three-dimensional consolidation, *J. Appl. Phys.*, *12*, 155–164.
Birkelo, B., K. Cieslik, B. Witten, S. Montgomery, B. Artman, D. Miller, and M. Norton (2012), High-quality surface microseismic data illuminates fracture treatments: A case study in the Montney, *Leading Edge*, *31*, 1318–1325.
Carslaw, H., and J. Jaeger (1959), Conduction of heat in solids.
Chang, K. W., and P. Segall (2016), Injection-induced seismicity on basement faults including poroelastic stressing, *J. Geophys. Res. Solid Earth*, *121*, 2708–2726, doi:10.1002/2015JB012561.
Detournay, E., and H.-D. C. Alexander (1993), Fundamentals of poroelasticity, in *Comprehensive Rock Engineering: Principles, Practice and Projects*, vol. 2, edited by C. Fairhurst, pp. 113–171, Pergamon Press, New York.
Dieterich, J. (1994), A constitutive law for rate of earthquake production and its application to earthquake clustering, *J. Geophys. Res.*, *99*(B2), 2601–2618.
Dinske, C. (2010), Interpretation of fluid-induced seismicity at geothermal and hydrocarbon reservoirs of Basel and Cotton Valley, PhD thesis, Freie Univ., Berlin.
Durham, W. B., and B. P. Bonner (1994), Self-propping and fluid flow in slightly offset joints at high effective pressures, *J. Geophys. Res.*, *99*(B5), 9391–9399, doi:10.1029/94JB00242.
Ellsworth, W. (2013), Injection-induced earthquakes, *Science*, *341*, 1225942, doi:10.1126/science.1225942.
Gischig, V. S., and S. Wiemer (2013), A stochastic model for induced seismicity based on non-linear pressure diffusion and irreversible permeability enhancement, *Geophys. J. Int.*, *194*(2), 1229–1249, doi:10.1093/gji/ggt164.
Grasso, J.-R. (1992), Mechanics of seismic instabilities induced by the recovery of hydrocarbons, *Pure Appl. Geophys.*, *139*(3), 507–534, doi:10.1007/BF00879949.
Griggs, D. T. (1936), Deformation of rocks under high confining pressures: I. Experiments at room temperature, *J. Geol.*, *44*(5), 541–577.
Häring, M. O., U. Schanz, F. Ladner, and B. C. Dyer (2008), Characterisation of the Basel 1 enhanced geothermal system, *Geothermics*, *37*, 469–495.
Healy, J. H., W. W. Rubey, D. T. Griggs, and C. B. Raleigh (1968), The Denver earthquakes, *Science*, *161*(3848), 1301–1310.
Hsieh, P. A., and J. D. Bredehoeft (1995), A reservoir analysis of the Denver earthquakes: A case of induced seismicity, *Energy Convers. Manage.*, *36*(6–9), 535–538.
Hummel, N. (2013), Pressure-dependent hydraulic transport as a model for fluid induced earthquakes, PhD thesis, FU Berlin.
Hummel, N., and S. Shapiro (2016), Back front of seismicity induced by non-linear pore pressure diffusion, *Geophys. Prospect.*, *64*(1), 170–191, doi:10.1111/1365-2478.12247.
Hummel, N., and S. A. Shapiro (2012), Microseismic estimates of hydraulic diffusivity in case of non-linear fluid-rock interaction, *Geophys. J. Int.*, *188*(3), 1441–1453.
Hummel, N., and S. A. Shapiro (2013), Nonlinear diffusion-based interpretation of induced microseismicity: A Barnett Shale hydraulic fracturing case study, *Geophysics*, *78*, B211–B226, doi:10.1190/geo2012-0242.1.
Jaeger, J. C., N. G. W. Cook, and R. W. Zimmermann (2007), *Fundamentals of Rock Mechanics*, 4th ed., 475 pp., Wiley-Blackwell, Malden, Mass.
Katsube, T. J., B. S. Mudford, and M. E. Best (1991), Petrophysical characteristics of shales from the Scotian shelf, *Geophysics*, *56*(10), 1681–1689, doi:10.1190/1.1442980.
King, V., L. Block, and C. Wood (2016), Pressure/flow modeling and induced seismicity resulting from two decades of high-pressure deep-well brine injection, Paradox Valley, Colorado, *Geophysics*, *81*(5), B119–B134, doi:10.1190/GEO2015-0414.1.
Knuth, D. E. (1998), *The Art of Computer Programming*, Addison-Wesley Longman, Reading, Mass.
Kraft, T., and N. Deichmann (2014), High-precision relocation and focal mechanism of the injection-induced seismicity at the Basel EGS, *Geothermics*, *52*, 59–73.
Lagarias, J. C., J. A. Reeds, M. H. Wright, and P. E. Wright (1998), Convergence properties of the Nelder-Mead simplex method in low dimensions, *SIAM J. Optim.*, *9*(1), 112–147.
Langenbruch, C., and S. Shapiro (2014), Gutenberg-Richter relation originates from Coulomb stress fluctuations caused by elastic rock heterogeneity, *J. Geophys. Res. Solid Earth*, *119*, 1220–1234, doi:10.1002/2013JB010282.
Li, M., Y. Bernabé, W.-I. Xiao, Z.-Y. Chen, and Z.-Q. Liu (2009), Effective pressure law for permeability of E-bei sandstones, *J. Geophys. Res.*, *114*, B07205, doi:10.1029/2009JB006373.
Mader, D. (1989), *Hydraulic Proppant Fracturing and Gravel Picking*, vol. 26, pp. 173–174, Elsevier Sci., Amsterdam, Netherlands.
Majer, E. L., R. Baria, M. Stark, S. Oates, J. Bommer, B. Smith, and H. Asanuma (2007), Induced seismicity associated with Enhanced Geothermal Systems, *Geothermics*, *36*(3), 185–222, doi:10.1016/j.geothermics.2007.03.003.
Miller, S. A. (2015), Modeling enhanced geothermal systems and the essential nature of large-scale changes in permeability at the onset of slip, *Geofluids*, *15*(1–2), 338–349, doi:10.1111/gfl.12108.
Miller, S. A., C. Collettini, L. Chiaraluce, M. Cocco, M. Barchi, and B. J. P. Kaus (2004), Aftershocks driven by a high-pressure CO_2 source at depth, *Nature*, *427*, 724–727, doi:10.1038/nature02251.
Parotidis, M., S. A. Shapiro, and E. Rothert (2004), Back front of seismicity induced after termination of borehole fluid injection, *Geophys. Res. Lett.*, *31*, L02612, doi:10.1029/2003GL018987.
Paterson, M. S., and T.-F. Wong (2005), *Experimental Rock Deformation—The Brittle Field*, Springer, Berlin.
Raleigh, C. B., J. H. Halej, and J. D. Bredehoeft (1972), Faulting and crustal stress at Rangely, Colorado, in *Flow and Fracture of Rocks, Geophys. Monogr. Ser.*, vol. 16, pp. 275–284, AGU, Washington, D. C., doi:10.1029/GM016p0275
Raleigh, C. B., J. H. Halej, and J. D. Bredehoeft (1976), An experiment in earthquake control at rangely, Colorado, *Science*, *191*, 1230–1237.
Rice, J. R. (1992), Fault stress states, pore pressure distribution, and the weakness of the San Andreas Fault, in *Fault Mechanics and Transport Properties of Rock*, edited by B. Evans and T. F. Wong, pp. 476–503, Academic Press, San Diego, Calif.
Rothert, E., and S. A. Shapiro (2003), Microseismic monitoring of borehole fluid injections: Data modeling and inversion for hydraulic properties of rocks, *Geophysics*, *68*, 685–689.
Rothert, E., and S. A. Shapiro (2007), Statistics of fracture strength and fluid-induced microseismicity, *J. Geophys. Res.*, *112*, B04309, doi:10.1029/2005JB003959.
Rozhko, A. Y. (2010), Role of seepage forces on seismicity triggering, *J. Geophys. Res.*, *115*, B11314, doi:10.1029/2009JB007182.

Rutqvist, J., J. Birkholzer, and C.-F. Tsang (2008), Coupled reservoir-geomechanical analysis of the potential for tensile and shear failure associated with CO_2 injection in multilayered reservoir-caprock systems, *Int. J. Rock Mech. Min. Sci.*, *45*, 132–143.

Segall, P. (1989), Earthquakes triggered by fluid extraction, *Geology*, *17*, 942–946.

Segall, P., and S. Lu (2015), Injection-induced seismicity: Poroelastic and earthquake nucleation effects, *J. Geophys. Res. Solid Earth*, *120*, 5082–5103, doi:10.1002/2015JB012060.

Shapiro, S. (2015), *Fluid-Induced Seismicity*, Cambridge Univ. Press, Cambridge, U. K.

Shapiro, S. A. (2012), Comment on "Role of seepage forces on seismicity triggering", *J. Geophys. Res.*, *117*, B03305, doi:10.1029/2011JB008346.

Shapiro, S. A., and C. Dinske (2009), Scaling of seismicity induced by nonlinear fluid-rock interaction, *J. Geophys. Res.*, *114*, B09307, doi:10.1029/2008JB006145.

Shapiro, S. A., E. Huenges, and G. Borm (1997), Estimating the permeability from fluid-injection induced seismic emission at the KTB site, *Geophys. J. Int.*, *131*, F15–F18.

Shapiro, S. A., P. Audigane, and J.-J. Royer (1999), Large-scale in situ permeability tensor of rocks from induced microseismicity, *Geophys. J. Int.*, *137*, 207–213.

Shapiro, S. A., E. Rothert, V. Rath, and J. Rindschwentner (2002), Characterization of fluid transport properties of reservoirs using induced microseismicity, *Geophysics*, *67*, 212–220.

Shapiro, S. A., R. Niemann, G. P. Khizhniak, Y. P. Ilyushin, V. V. Plotnikov, and S. V. Galkin (2015), Stress-dependent permeability versus stiff and compliant porosity: Theory and experiments,SEG Technical Program Expanded Abstracts SEG–2015-5761906, presented at 2015 SEG Annual Meeting, pp. 2990–2994, Society of Exploration Geophysicists, New Orleans, Louisiana, 18–23 Oct., doi:10.1190/segam2015-5761906.1.

Suckale, J. (2009), Induced seismicity in hydrocarbon fields, in *Advances in Geophysics*, vol. 51, edited by R. Dmowska, pp. 55–106, Academic Press, USA.

Talwani, P., and S. Acree (1984), Pore pressure diffusion and the mechanism of reservoir-induced seismicity, *Pure Appl. Geophys.*, *122*(6), 947–965, doi:10.1007/BF00876395.

Terzaghi, K. (1936), The shearing resistance of saturated soils and the angle between planes of shear, paper presented at 1st International Conference on Soil Mechanics and Foundation Engineering, vol. 1, pp. 54–56, Harvard Univ. Press, Cambridge, Mass.

Van Wees, J. D., L. Buijze, K. Van Thienen-Visser, M. Nepveu, B. B. T. Wassing, B. Orlic, and P. A. Fokker (2014), Geomechanics response and induced seismicity during gas field depletion in the Netherlands, *Geothermics*, *52*, 206–219, doi:10.1016/j.geothermics.2014.05.004.

Zoback, M., and H. P. Harjes (1997), Injection-induced earthquakes and crustal stress at 9 km depth at the KTB deep drilling site, Germany, *J. Geophys. Res.*, *102*, 18,477–18,491.

Zoback, M. D., and J. C. Zinke (2002), Production-induced normal faulting in the Valhalland Ekofisk oil fields, *Pure Appl. Geophys.*, *159*, 403–420.